Self-Assembly of Ordered Nanowires in Biological Suspensions of Single-Wall Carbon Nanotubes

Erik K. Hobbie,[†,*] Jeffrey A. Fagan,[†] Matthew L. Becker,[†] Steven D. Hudson,[†] Nikta Fakhri,[‡] and Matteo Pasquali[‡]

[†]Polymers Division, National Institute of Standards and Technology, Gaithersburg, Maryland 20899, and [‡]Department of Chemical and Biological Engineering, Rice University, Houston, Texas 77251

ABSTRACT We investigate the self-assembly of ordered nanowires from length-purified single-wall carbon nanotubes (SWCNTs) in aqueous suspensions of the biological surfactant sodium deoxycholate. Macroscopically straight and nearly periodic linear arrangements of aligned individual SWCNTs are found to self-assemble in two-dimensional geometries from nanotube suspensions that are otherwise stable in the bulk, which we attribute to a dominance of surface effects under strong confinement. Directed self-assembly is explored through surface patterning, opening up new potential routes to nanotube manipulation for optical diagnostics and applications that require ordered arrangements of mutually aligned SWCNTs. The stability of these structures to thermal fluctuations and changes in solution chemistry are surveyed with near-infrared fluorescence microscopy.

KEYWORDS: single-wall carbon nanotubes · biological surfactants · self-assembly · near-infrared photoluminescence

The ability to efficiently arrange anisotropic nanoparticles into ordered mesoscale patterns is critical to many emerging applications in nanotechnology, including microelectronic circuits, optical sensors, and structural composites. The most promising route to this is self-assembly, or the spontaneous formation of microscopically ordered superstructures through the combined effects of enthalpy and entropy.[1] Such a progression is intimately linked to the broader topic of phase transitions and critical phenomena, being driven by changes in the appropriate free energy, which depends on internal energy U and entropy S. At the transition, the lower entropy of the more ordered self-assembled state implies that there must be an overall decrease in the total internal energy, for example, which is dominated by the form of the interparticle potential. On their own, however, nanoparticles are notoriously difficult just to disperse, particularly when they possess significant shape anisotropy. Strong Van der Waals forces dominate U and substantial surface modification is often required before colloidal self-assembly can become a viable option.

In the search for new approaches, biology provides both insight and inspiration. Nature excels at the precise placement and orientation of nanoscale components out of initially disordered configurations.[2] A simple but compelling example of this can be found in the so-called bile salts or bile acids. Produced in the liver through the oxidation of cholesterol and stored in the gallbladder, these steroidal acids play a critical role in digestion, including the solubilization of fat through the formation of mixed-lipid micelles.[3] As amphiphiles they are uniquely structured with a convex hydrophobic surface and a concave hydrophilic face containing a varied number of hydroxyl (OH) groups,[4] and they thus exhibit a rich and complex phase behavior in aqueous solution. The primary micelle is small with an average size of 1 nm, but at higher concentrations these subunits associate into larger rodlike aggregates.[5] Changes in pH, ionic strength, temperature, or surfactant concentration can trigger the self-assembly of these secondary units into hydrated nanoribbons or nanotubes with macroscopic persistence lengths [6−8] and hydrated fibrils that can exhibit hexagonal liquid-crystalline order at high surfactant concentrations.[9]

Bile salts have recently been demonstrated to be extremely efficient at dispersing single-wall carbon nanotubes (SWCNTs) in aqueous solution.[10] The SWCNTs naturally reside within the hydrophobic core of the rodlike molecular aggregate, leading to a unique surfactant coating that exceeds single-stranded DNA in its effectiveness and is orders-of-magnitude cheaper. This has contributed to the development of new SWCNT-based biological sensor technologies,[11] as well as scalable length[12] and

*Address correspondence to erik.hobbie@nist.gov.

Received for review September 23, 2008 and accepted December 01, 2008.

Published online December 16, 2008.
10.1021/nn800609y CCC: $40.75

chirality[13] SWCNT separation schemes. One might expect that new routes to nanotube manipulation can be found by exploiting the natural tendency for these and other biological molecules to self-assemble. Here, we show that SWCNTs stabilized in bile-salt solutions can spontaneously self-assemble into highly ordered and macroscopically long nanowires that might offer promise for a host of potential applications. We suggest that geometrical confinement is critical to this effect, which we quantify in the form of a phase diagram. We also explore the directed assembly of these wires on patterned surfaces and investigate their response to thermal fluctuations and changes in solution pH. Our objective here is to quantify and characterize the phase behavior associated with the self-assembly process and relate the bulk equilibrium morphology to the unique linear structures observed in confined suspensions. From this foundation, we investigate and discuss some potential routes toward directed self-assembly, which would be a critical step in realizing potential applications.

RESULTS AND DISCUSSION

Single-wall carbon nanotubes (SWCNTs) have received considerable attention because of their outstanding optical, electronic, mechanical, and thermal characteristics.[14] The electronic and optical properties of these materials are dictated by their electronic band structure, which is specified by the chiral vector (*n*,*m*) characterizing the symmetry of rolling a 2D graphene sheet into a hollow tube of diameter *a*. Here, we use raw material that has a natural enrichment in the (6,5) and (7,5) semiconducting species. These SWCNTs have a band gap defined by cusp-like singularities in the electronic density of states arranged symmetrically on either side of the Fermi level,[15] denoted 11, 22, 33, *etc.* in order of increasing energy. In isolation, their optical absorption spectra show sharp peaks associated with electronic interband transitions.[15−17] A particularly intriguing consequence of this is a fluorescent emission triggered by the absorption of a photon across the 22 and the subsequent re-emission across the 11.[16,17] For small diameter semiconducting SWCNTs, this intrinsic photoluminescence occurs in the near-infrared (NIR), a region of the electromagnetic spectrum where biological fluids and materials are relatively transparent.[18]

To prepare the samples, dry material was tip sonicated in 2% aqueous solutions of the bile-salt sodium deoxycholate (DOC) followed by light centrifugation to remove large bundles and impurities. The primary critical-micelle-concentration (CMC) for DOC occurs at around 0.05%, with a secondary CMC at around 0.1%.[5] The strength of the semiconducting SWCNT optical resonances, the brightness of the NIR photoluminescence, and the quantum yield all appear to increase with nanotube length,[19−21] and the samples were further separated by length using the ultracentrifugation technique developed by Fagan et al.[12] The stock suspensions used in this study represent the longest SWCNTs in the initial suspensions and are characterized in Figure 1. They have a mean length of 1 μm as measured by atomic-force microscopy (AFM) and depolarized dynamic light scattering (DLS) and a diameter of around 1 nm as determined by AFM on ethanol-rinsed suspensions. The standard deviation around the mean length is approximately 100 nm based on AFM from an ensemble of 150 nanotubes. The 11 and 22 absorption peaks for the dominant (6,5) semiconducting species are indicated in Figure 1a, with the subdominant peak to the right of these features representing the (7,5) SWCNT. The absorption at 500−700 nm makes the suspension blue (Figure 1b) at this concentration, and the emission spectra (Figure 1c) show strong features in the NIR from the two dominant semiconducting species.

To quantify the phase behavior, the initial stock suspension was partitioned into smaller samples with 0.01 μg/ml $< \phi_{SWCNT} <$ 10 μg/ml and 0.1% $< \phi_{DOC} <$ 20% where ϕ_{SWCNT} is the concentration of nanotubes and ϕ_{DOC} is the mass concentration of bile salt. Samples were also prepared at $\phi_{SWCNT} = 0$ over the same range of ϕ_{DOC}. All measurements described here were performed at ambient temperature (25 °C). At higher temperatures (above 40 °C), macroscopic structures in bulk DOC suspensions disappeared and the solutions became transparent, consistent with the bulk phase diagram reported in ref 9. Below the biphasic liquid-crystalline binodal at *ca.* 15% DOC,[9] all suspensions studied remained stable and optically homogeneous in the bulk over a time scale of months. Small amounts of each suspension were sealed between a glass slide and coverslip (approximate thickness, $h = 10$ μm) using vacuum grease. Alternatively, unsealed samples were annealed in a 100% humid environment consisting of a tightly sealed 1 L chamber containing mostly water with the samples resting on a platform just above the water level. Different approaches were used to treat the surface of the slides prior to loading the sample as described in greater detail below. The confined suspensions were annealed for 3−5 days prior to observation. The primary characterization techniques employed to evaluate the morphology were polarized bright-field optical microscopy, polarized NIR fluorescence microscopy (with a 60x PlanApo 1.2 NA water-immersion objective, a liquid-nitrogen cooled InGaAs CCD, and band-pass optics dictated by the absorption and emission spectra in Figure 1), and transmission electron microscopy (TEM) on rinsed and dried samples.

The different morphologies are summarized in Figure 2. A striking observation was the formation of macroscopic fibrils in neat DOC solutions (Figure 2a) that were optically homogeneous in the bulk. Rotating a quarter-wave plate between the polarizers and monitoring the color change identifies the slow optical axis

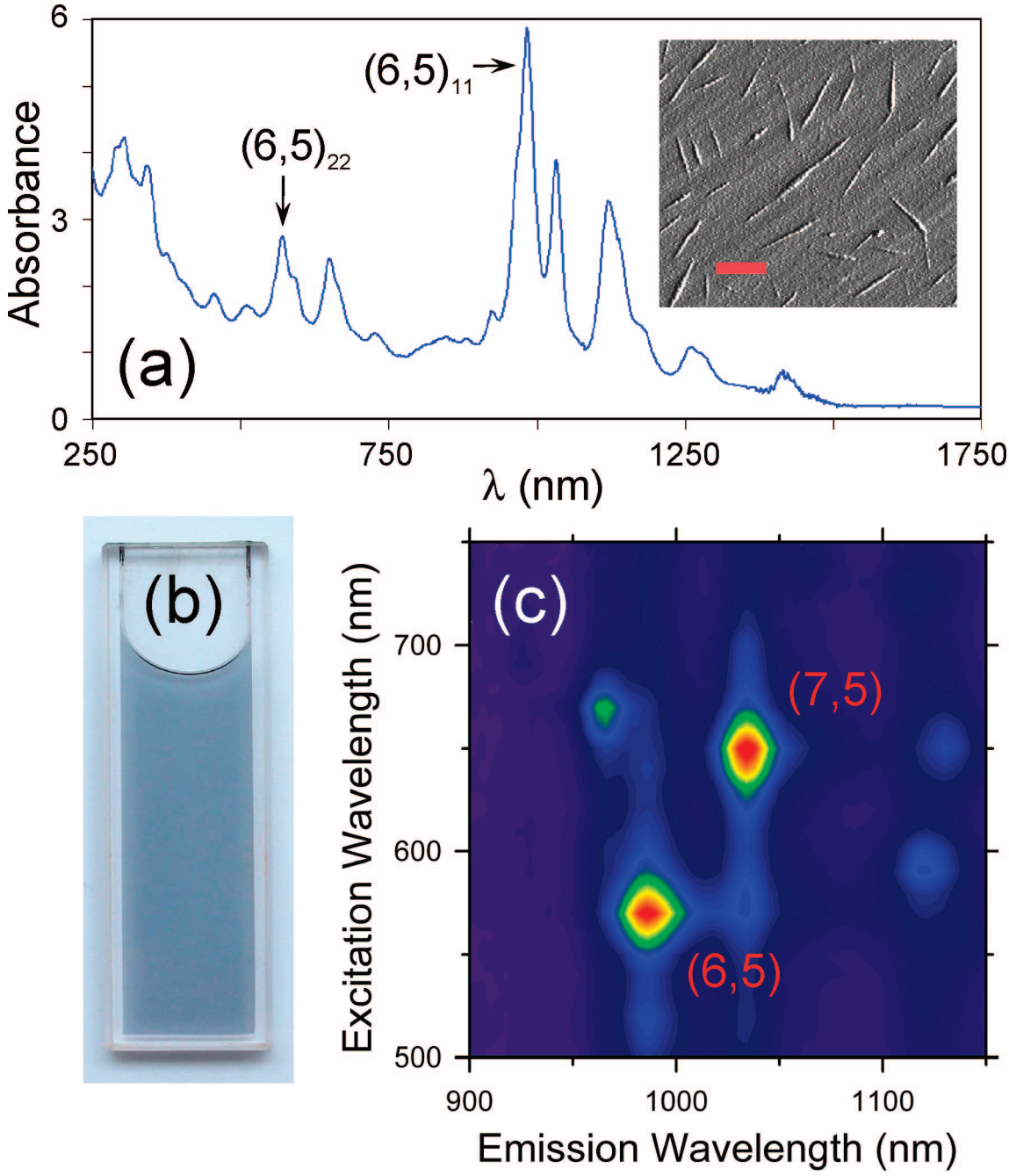

Figure 1. (a) Optical absorption spectrum of length-purified SWCNTs showing the first (11) and second (22) interband transition of the dominant (6,5) semiconducting species. The inset shows a typical AFM image of the micelle-encapsulated nanotubes on mica (scale bar = 1 μm). (b) The strong 22 absorption features of the (6,5) and (7,5) SWCNT at 500−600 nm make the 2% DOC, 7 μg/ml SWCNT suspension blue. (c) Band-gap fluorescence map of the same suspension, where the two bright features correspond to the intrinsic NIR emission from excitation at the 22 absorption peaks in panel a.

of the fibril as its director (arrow, Figure 2b). Fibrils with similar optical properties have been observed in more highly concentrated bulk bile-salt solutions as liquid-crystalline precursors.[9] In these fibrils, rodlike micelle subunits are condensed and oriented parallel to the fibril axis. They form through the combination of facial hydrophobic−hydrophilic interactions and intermicelle hydrogen bonding mediated by changes in temperature or concentration.[9] We propose that their formation here at concentrations well below the biphasic liquid-crystalline transition is intimately linked to the geometrical confinement of the suspensions, as discussed in further detail below.

Individual SWCNTs encapsulated in DOC are apparent as bright diffraction-limited spots in NIR fluorescent microscopy (Figure 2b). When the SWCNT concentration in confinement is sufficiently low, these individuals get incorporated into the self-assembled fibrils, as shown in Figure 2c. Individual semiconducting SWCNTs appear remarkably to be somewhat peri-

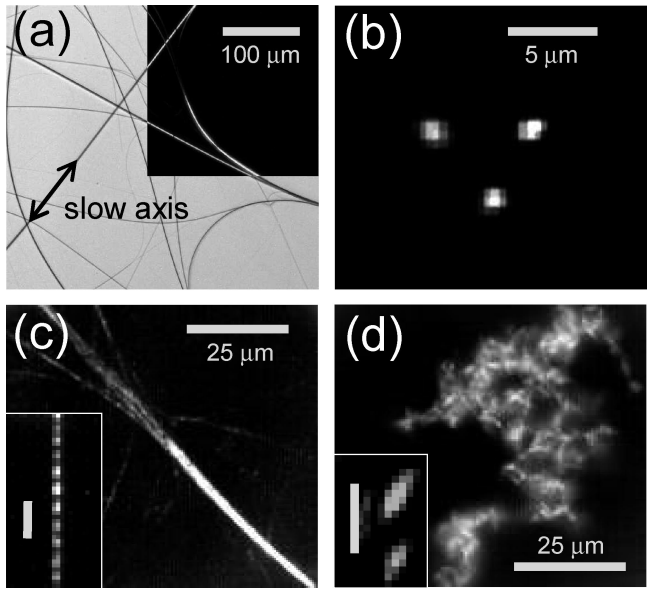

Figure 2. (a) Pure DOC fibrils assembled in confined bile-salt suspensions (2% DOC), where the birefringence (crossed polarizers, upper right quadrant) arises from the alignment of rodlike micelles along the axis of the fibril. Extinction is observed when the fibril is vertical (see inset) or horizontal, that is, parallel to either of the crossed polarizers. (b) NIR fluorescent micrograph of individual Brownian SWCNTs encapsulated in bile-salt. (c) Under confinement, the DOC encapsulated SWCNTs are incorporated into self-assembled fibrils (2% DOC, 0.35 μg/ml SWCNT) with a nearly periodic arrangement of fluorescent nanotubes within each strand (inset, scale bar = 5 μm, 2% DOC, 1.5 μg/ml SWCNT). (d) Above a critical surfactant concentration, the encapsulated SWCNTs self-assemble into compact tactoids (inset, scale bar = 5 μm, 7.3% DOC, 5.5 μg/ml SWCNT) that aggregate into larger clusters (12% DOC, 9 μg/ml SWCNT). All suspensions are stable and homogeneous in the bulk.

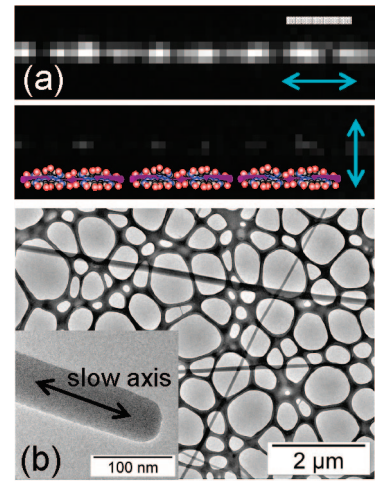

Figure 3. (a) A SWCNT fibril imaged in the NIR with the excitation polarized nearly parallel (top) and nearly perpendicular (bottom) to the axis of orientation (scale bar = 5 μm, 1% DOC, 3.5 μg/ml SWCNT). The inset shows a schematic picture of the possible relative arrangement of semiconducting nanotubes within a strand suggested by the apparent arrangement of bright and dark spots within a fibril. The dark regions likely represent a combination of SWCNT-free regions of assembled surfactant and nonluminescent metallic tubes. (b) TEM images of solid long straight SWCNT composite wires obtained after rinsing away the excess bile salt on a lacey carbon support.

odically arranged within the single strand of a fibril (inset, Figure 2c) and these strands further associate into macroscopic wires with a bright NIR fluorescent signal. Micrometer-scale dark regions periodically interspersed between bright spots within single fibrils (inset, Figure 2c) suggest either SWCNT-free regions of assembled DOC or nonluminescent metallic SWCNTs interspersed between successive semiconducting SWCNTs. The stoichiometry of nonluminescent metallic *vs* luminescent semiconducting SWCNTs is roughly expected to be between 10:90 and 30:70 for the refined SWCNT material used here. This would seem to slightly favor the first scenario, which could be explained by a dependence of the effective intermicelle hydrogen-bonding potential on the presence or absence of encapsulated SWCNT. For a relatively complex surfactant like DOC, slight differences in the packing of DOC molecules around a nanotube could lead to subtle changes in the effective interparticle potential that might favor a nearly periodic linear arrangement of encapsulated SWCNTs interspersed with (SWCNT-free) pure-surfactant "voids". An intriguing and unresolved question is the location of the metallic SWCNTs within the assembled fibrils. For the anticipated minority metallic content, the luminescently "dark" metallic SWCNTs would likely show up as polydispersity in the length of dark segments and deviations from a periodic arrangement of luminescent segments.

When the hydrophilicity of the glass slides is enhanced through ultraviolet-ozone plasma etching, the SWCNT fibrils and subsequent wires stick to the confining surfaces. When these surfaces are made hydrophobic through the deposition of an organo-silane self-assembled monolayer (SAM), the SWCNT fibrils exhibited a greater tendency to extend throughout the bulk of the confined layer. A high degree of SWCNT alignment within the fibrils is apparent in polarized NIR fluorescence microscopy (Figure 3a), and TEM performed on extracted, rinsed, and dried fibrils (Figure 3b) reveals solid SWCNT-DOC wires that are macroscopically long, uniform, and straight. Above a bile-salt concentration of around 4%, still well below the biphasic binodal in the bulk pure DOC solutions, the SWCNT fibrils give way to diffuse clusters of compact SWCNT aggregates that have a tactoidal appearance, as shown in Figure 2d. Pure DOC suspensions over this range of bile-salt concentration nucleate liquid-crystalline and crystalline domains in confinement.

These observations are summarized as a phase diagram in Figure 4a. Green markers denote confined suspensions of individual Brownian SWCNTs, blue markers denote fibrils, and red markers denote macroscopically disordered aggregates, where all the data correspond to three days of annealing. Phase boundaries are diffuse, and individual SWCNTs, both mobile and immobile adhered to the glass surfaces, coexist with the heterogeneous phases. The light blue dotted line indicates the interval of ϕ_{DOC} where fibrils form under confine-

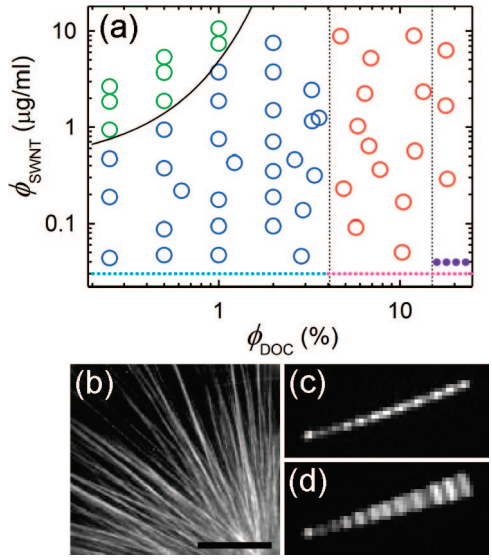

Figure 4. (a) Phase diagram in the plane of nanotube and bile-salt concentration delineating regions of dispersed individual SWCNTs (green), fibrils (blue), and disordered aggregates (red) for the confined suspensions. For $\phi_{SWCNT} = 0$, fibrils form under confinement in the DOC concentration interval delineated by the blue dotted line and compact liquid-crystalline and crystalline domains nucleate in the interval denoted by the pink dotted line. In bulk suspensions, biphasic liquid-crystalline order emerges at DOC concentrations indicated by the purple dotted line. Curvature in the upper-left phase boundary suggests more than one critical micelle concentration (CMC) with increasing DOC content. (b) Treating the confining surfaces with a hydrophobic SAM leads to the nucleation of dense starlike clusters from specific sites in the SAM (scale bar = 25 μm, 1% DOC, 3.5 μg/ml SWCNT). (c) A single fibril and (d) a superposition of 500 temporally successive frames taken at 0.05 s intervals showing limited thermal bending (1% DOC, 3.5 μg/ml SWCNT).

ment in pure DOC suspensions. The dotted pink line denotes the nucleation of ordered domains under confinement but not in the bulk, and the dotted purple line indicates bulk liquid-crystalline order. Increasing the annealing time beyond three days slightly increases the extent of fibril formation across both phase boundaries, suggesting that both the dispersed and disordered phases are metastable with respect to fibril formation. Increasing the annealing time also leads to more static and straight structures, as well as a higher fraction of fibrils and individual SWCNTs attached to the confining surfaces.

The critical role of geometric confinement can be heuristically understood as follows. The total free energy F will be the sum of two terms F_b and F_s representing bulk and surface contributions, respectively. The ratio F_s/F_b scales as $1/h$ and F_s will thus dominate for small h. For low SWCNT concentrations, the fibrils most likely nucleate from defect sites on the surfaces. Treating the glass slides with a hydrophobic SAM leads to strong nucleation at specific sites which likely correspond to defects in the SAM (Figure 4b). In a simple sense, these defect sites can be viewed as fluctuations in local pH that are "quenched" onto the confining surfaces, which in turn trigger the local nucleation of ordered domains. The crossover in Figure 4 between fibrils and disordered aggregates with increasing DOC concentration thus mirrors the change in morphology encountered upon moving deeper into the ordered region of the bulk DOC phase diagram along an isotherm of increasing concentration.[9] The region of true dispersion in the upper left part of Figure 4 reflects the isotropic part of the bulk phase diagram, with the somewhat counterintuitive observation of better SWCNT dispersion at lower DOC and higher SWCNT concentrations. This could be because the SWCNTs act as a sink for free DOC, effectively lowering the concentration of free bile salt that can initiate a nucleation event. It could also occur because there is not enough surfactant to fully cover the SWCNTs, which might inhibit DOC-mediated self-assembly. Figure 4c shows a fibril with one end attached to the SAM-coated glass surface with the remaining segments free to thermally diffuse. A temporal superposition of 500 images taken at 20 Hz (Figure 4d) reveals thermal motion dominated by orientational diffusion of the entire fibril with weak bending undulations that suggest significant stiffness in the self-assembled composite fibril. A quantitative analysis of these images provides an approximate fibril persistence length of 200−300 μm for the fibril shown in Figure 4d.

An important question for potential applications is how to template and direct the fibril growth on a macroscopic scale. Several approaches were explored in this regard. Our first efforts were focused on microscale capillary printing of simple linear patterns as a way to try to modulate the growth of the SWCNT structures. A polydimethylsiloxane (PDMS) rubber stamp with parallel micrometer wide channels was fabricated using conventional soft lithographic techniques and used to print parallel lines of water-soluble polymer (either poly(acrylic acid) or fructose) on glass slides that had been exposed to a UVO plasma to both clean the confining surfaces and increase their hydrophilicity (Figure 5a). Dilute polymer solutions were used because the low viscosity ensured that the templating polymer solution uniformly filled the microscale channels. After the water had evaporated, the stamp was removed to reveal the uniform polymer features shown in Figure 5a. These polymer-patterned surfaces were further dried under vacuum and then uniformly covered with the hydrophobic SAM, such that rinsing away the polymer left only hydrophilic lines interspersed on a hydrophobic SAM-covered background. Finally, the SWCNT-DOC solution was introduced between the patterned template and a homogeneously hydrophobic coverslip and the sample was annealed. As an alternative approach, we also used the same PDMS stamp placed on both hydrophilic and SAM-treated slides to print the DOC/SWCNT solutions directly onto the same linear pattern. Again, dilute SWCNT solutions were used to ensure that the suspension rapidly and uniformly filled the chan-

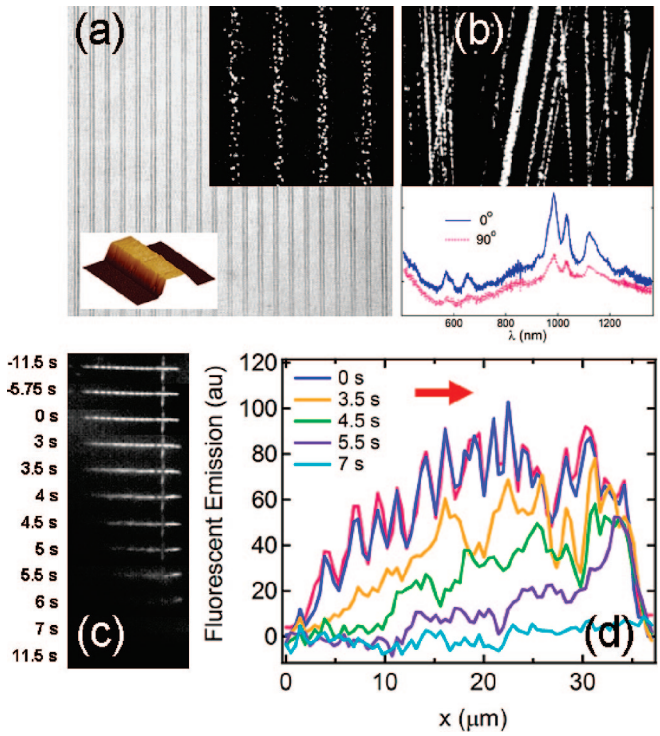

Figure 5. (a) Attempts at patterning fibril nucleation using microcapillary printing with a PDMS stamp by either printing a template or printing the SWCNT suspension directly leads to limited fibril growth due to reduced access to nucleation sites with a predominant occurrence of individual SWCNTs (inset, 1% DOC, 3.5 μg/ml SWCNT). (b) Patterning the surface by rubbing or abrading one of the confining surfaces, in contrast, is an effective way to pattern a degree of fibril growth (1% DOC, 7.5 μg/ml SWCNT). (c) Time-dependent distortion and quenching of fibril PL by a diffusing chemical front of 0.1 M NaOH, where the contrast of each image has been adjusted to achieve a common dark background to offset a temporally transient brighter background due to the transport of many individual, unquenched (NIR luminescent) SWCNTs. (d) Linear intensity profiles of the time-dependent sequence in panel c, where the arrow indicates the diffusion direction of the NaOH gradient (1% DOC, 3.5 μg/ml SWCNT).

nels in the PDMS stamp. These samples were then annealed in 100% humidity environments for the appropriate duration with the stamp in place. Although some localized fibril formation was achieved using both of these approaches, typical patterns contained individual SWCNTs deposited on the surface, as shown in the upper right inset to Figure 5a.

A much more effective, although less-controlled approach was to simply rub the SAM-treated surface with a fine abrasive (1 μm aluminum-oxide particle polishing film) prior to loading the sample, which produced nearly parallel continuous lines of self-assembled SWCNT wires up to 1.5 mm in length (Figure 5b). Similar linear patterns could also be obtained by scoring the SAM-treated glass surface with a carbide tip prior to loading the SWCNT-DOC suspension, and some success was also achieved by just directionally wiping cleaned but otherwise untreated glass surfaces with ethanol and a paper tissue. Polarized optical absorption spectroscopy on such films (lower panel, Figure 5b) also suggests SWCNT alignment within fibrils, where absorption features at 90° polarization are attributed to deviations from a parallel arrangement of wires and a component of isotropically oriented "free" SWCNTs.

The observations outlined in the above two paragraphs are somewhat intuitive. In our first approach, patterning the surface through microcapillary printing of a removable polymer and the introduction of a uniform SAM will restrict the number of surface nucleation sites available to the confined SWCNT-DOC suspensions by effectively masking the majority of these with the SAM. Similarly, directly printing the SWCNT suspension through the narrow linear channels of the PDMS stamp onto a hydrophilic slide also restricts the access of individual DOC-encased SWCNTs to nucleation sites. In both instances, fibril formation would be suppressed. In contrast, directly rubbing a homogeneously hydrophobic SAM-treated surface likely introduces a large number of linear microscale patterns containing many nucleation sites on the confining surface, all of which should be accessible to the confined SWCNT suspension.

Finally, we demonstrate the sensitivity of the NIR photoluminescence and structural stability of a fibril to changes in local pH by optically monitoring the diffusive motion of a chemical front along the axis of a fibril, as shown in Figure 5c,d. A solution of 0.1 M NaOH in water was introduced to one unsealed side of a confined sample and the diffusion of the chemical front into the aqueous DOC-SWCNT suspension was optically monitored by tracking the structure and NIR emission of an oriented fibril as a function of time (Figure 5c). The traces in Figure 5d are background-corrected spatial intensity profiles of the NIR emission along the fibril, where *x* is the direction of chemical diffusion. Initially, the PL from the individual semiconducting SWCNTs composing the fibril is apparent as a periodic variation in emission intensity along the fibril axis. As the NaOH diffuses along the fibril it both destabilizes the structure and quenches the PL of individual SWCNTs, leading to loss of resolution and a gradient in intensity (Figure 5d). Performing the same experiment with 2% DOC solutions or distilled water as the intrusive fluid led to the deformation and partial breakup of fibrils with no quenching of the NIR emission from the individual semiconducting SWCNTs.

CONCLUSIONS

We have investigated the self-assembly of ordered nanowires of aligned SWCNTs in a biological surfactant, where self-assembly occurs through a combination of facial ampiphillic effects and hydrogen bonding in confined suspensions. Macroscopically straight and mechanically stiff nanowires containing well-aligned and nearly periodic arrangements of individual SWCNTs are found to nucleate from surface defect sites in 2D confined suspensions. A degree of directed nucleation is achieved through surface patterning, opening up po-

tential new routes to nanotube manipulation and self-assembly. The approach is immediately suitable as an optical platform for spectroscopic diagnostics that require large ensembles of mutually aligned SWCNTs, and it potentially offers a promising new approach to carbon-nanotube self-assembly for microelectronic, optical-sensing, and composite applications that rely on the precise placement, orientation, and arrangement of individual single-wall carbon nanotubes on surfaces.

METHODS

Materials. Cobalt-molybdenum-catalyst (CoMoCat) SWCNTs were dispersed in aqueous stock solution using 2% by mass sodium deoxycholate surfactant (DOC). SWCNT solution preparation consisted of sonication (tip sonicator, 0.64 cm) of the SWCNT powder loaded at (1.0 ± 0.1) mg/mL in the 2% surfactant solution for 1.5 h in 32 mL batches immersed in an ice−water bath at 30 W of applied power. Postsonication, each suspension was centrifuged at 21000*g* in 1.5 mL centrifuge tubes for 2 h, or 35000*g* for 2 h in 13 mL centrifuge tubes, and the supernatant was collected. Density modified solutions for length separation were generated by mixing the appropriate surfactant or SWCNT solution with an iodixanol, (5,5′-[(2-hydroxy-1-3 propanediyl)-bis(acetylamino)]bis[*N*,*N*′-bis(2,3dihydroxylpropyl-2,4,6-triiodo-1,3-benzenecarboxamide)]) and 2% by mass sodium deoxycholate solution. The layer densities were chosen such that $\Delta\rho \gg \Delta\rho_{SWNT}$ in the starting layer and for 5 cm above; a dense under-layer was also included. Stock suspensions contained from 0 to 10% iodixanol, the concentration of which scaled proportionally with ϕ_{SWCNT} upon dilution or concentration, with no obvious effect on the assembly.

A Beckman-Coulter L80-XP ultracentrifuge with a swinging bucket SW.32 Ti rotor was used with the SW-32 bucket sets for the length separation and postfractionation concentration of like fractions. The prepared (layered) centrifuge tube contained 24 mL of liquid in four layers: 1 mL of 40% iodixanol, 1 mL of 30% iodixanol, 2 mL of 20% iodixanol containing the SWCNTs, and 20 mL of 18% iodixanol in the top layer. All layers contained 2% sodium deoxycholate. Separation was performed at 1254 Rad/s for 96 h. After the separation, 16 individual fractions of 1.5 mL were collected by pipetting in 0.75 mL increments. Fraction 9 was extracted for this work and the mean SWCNT length was characterized by depolarized (*Vh*) dynamic light scattering and atomic force microscopy as described in ref 19. Different concentrations of SWCNT and surfactant were prepared by serial dilution of the stock suspensions or by forced-dialysis concentration. A consistent measure of SWCNT concentration for these initial stock suspensions was obtained by using the ratio of the absorbance at 775 nm from the sonicated, precentrifuged SWCNT suspension (for which the SWCNT mass fraction is precisely known) to the absorbance at 775 nm for the final fraction as a measure of SWCNT mass loss. The wavelength of 775 nm was chosen as it lies away from any optical resonance and is thus less sensitive to any apparent length-dependent optical effects.

Hydrophobic SAMs on glass were prepared by 48 h exposure of cleaned and UVO-treated glass microscope slides and coverslips to *n*-octyldimethylchlorosilane vapor in a sealed glass container under vacuum. Surfaces were then rinsed with dichloromethane, rinsed with distilled deionized water, and air-dried prior to use.

Optical Spectroscopy. UV/visible/near-infrared absorption spectroscopy was performed in transmission mode on a PerkinElmer Lambda 950 UV−vis−NIR spectrophotometer over the ranges of (1750 to 190) nm. For homogeneous suspensions, the incident light was depolarized prior to the sample compartment. For patterned films confined between glass microscope slides, the incident light was polarized with a Glan-Thompson polarizer. In both cases the measurement was corrected for the dark current and background spectra; data was recorded at 1 nm increments, with an instrument integration time of 0.2 s per increment. Additionally, the reference beam was left unobstructed, and the subtraction of the appropriate reference sample was performed during data reduction.

Fluorescence maps for stock SWCNT solutions were generated using a JY-Horiba Fluorolog-3 spectrofluorometer and corrected for the instrument's source spectral distribution and detector spectral response. Excitation wavelength was scanned in 3 nm increments using a 450 W xenon lamp through a 15 nm slit and a 1200 lines/mm monochromator with a 500 blaze. The emission was collected front face and measured using a liquid N_2-cooled InGaAs detector over 5 nm increments through a 15 nm slit and a 600 lines/mm monochromator with a 1500 blaze.

Microscopy. Tapping-mode atomic force microscopy (AFM) measurements of the isolated SWCNTs, printed textures, and SWCNT-loaded patterns were conducted in air using a Nanoscope IV system (Digital Instruments) operated under ambient conditions with standard silicon tips (NanoDevices Metrology Probes; 125 μm length; normal spring constant, 40 N/m; resonance frequency, 280−330 kHz). Surface patterns were prepared as described above and investigated after being allowed to dry after the PDMS stamp was removed to afford clear imaging conditions. Numerous images depicted well-defined patterns of the expected dimensions. For TEM characterization, the fibril suspensions were deposited from a syringe onto a lacey carbon support grid. The fibrils were washed briefly by touching the back side of the grid to a clean water drop and then to a filter paper edge. This washing and blotting was repeated several times before the specimen was allowed to dry. The sample was then examined by transmission electron microscopy, using a Philips EM400T, operated at 120 kV, in bright field and electron diffraction modes. Optical microscopy was performed on an Olympus IX71 inverted microscope using dichroic polarizers. NIR fluorescence imaging capability[22] was achieved using a 60× PlanApo 1.2 NA water-immersion objective, a liquid-nitrogen cooled InGaAs CCD, and band-pass optics dictated by the absorption and emission spectra in Figure 1.

The fibril bending rigidity is obtained from time-resolved NIR fluorescence microscopy by analyzing the fluctuating shape of the fibril using a Fourier decomposition technique.[23] The backbone coordinates of the fibril were determined with subpixel accuracy by an intensity-weighted analysis. The shape of the fibril in each image was expressed as a sum of cosine bending modes (which form an orthogonal basis); mode amplitudes were extracted by projecting the image shape onto these basis functions. In the absence of external forces the variance of the lower mode amplitudes is dominated by thermal bending fluctuations and, according to the equipartition theorem, can be related to the bending rigidity through

$$\langle (a_n(t))^2 \rangle = \frac{k_B T}{\kappa} \frac{L^2}{(n\pi)^2} \quad (1)$$

where a_n is the amplitude of mode number n, L is the fibril length, k_B is the Boltzmann constant, T is the temperature, and κ is the fibril bending rigidity. At longer lag times the variance of the mode amplitudes for smaller modes approaches the expected n^{-2} behavior[24] with a bending rigidity of 1.1×10^{-24} Nm^2 or, equivalently, a persistence length $L_p = \kappa/(k_B T) \approx 270$ μm for the fibril in Figure 4d. The rotational diffusion of the entire fibril is extracted from the autocorrelation of the projection of the tangent unit vector $u(t)$ by fitting this correlation function to the temporal decay $e^{-2D_r t}$. The temporally varying tangent angles were obtained from the mean slope of the fibril backbone

$$\theta = \tan^{-1}\left(\frac{df}{dx}\right) \quad (2)$$

where $f(x) = cx$ is a first-degree polynomial (linear) fit to the backbone coordinates. We obtain $D_r \approx 0.04\ s^{-1}$ which is slightly

higher than the predicted $D_r \approx 0.03\ s^{-1}$ (based on the bulk rotational diffusivity of a slender rod of known length), consistent with earlier measurements of rotational diffusivity of individual SWCNTs.[25]

Acknowledgment. Certain commercial equipment and materials are identified in this paper to adequately specify the experimental procedure. In no case does such identification imply recommendation by NIST nor does it imply that the material or equipment identified is necessarily the best available for this purpose.

REFERENCES AND NOTES

1. Whitesides, G. M.; Boncheva, M. Beyond Molecules: Self-Assembly of Mesoscopic and Macroscopic Components. *Proc. Natl. Acad. Sci. U.S.A.* **2002**, *99*, 4769–4774.
2. Lowe, C. R. Nanobiotechnology: The Fabrication and Applications of Chemical and Biological Nanostructures. *Curr. Opin. Struct. Biol.* **2000**, *10*, 428–434.
3. Russell, D. W. The Enzymes, Regulation and Genetics of Bile Acid Synthesis. *Annu. Rev. Biochem.* **2003**, *72*, 137–174.
4. Small, D. M. In *The Bile Acids: Chemistry, Physiology and Metabolism*; Nair, P. P., Kritchevsky, D., Eds.; Plenum Press: New York, 1971; Vol. 1, pp 249−356.
5. Lopez, F.; Samseth, J.; Mortensen, K.; Rosenqvist, E.; Rouch, J. Micro- and Macrostructural Studies of Sodium Deoxycholate Micellar Complexes in Aqueous Solutions. *Langmuir* **1996**, *12*, 6188–6196.
6. Jean, B.; Oss-Ronen, L.; Terech, P.; Talmon, Y. Monodisperse Bile-Salt Nanotubes in Water: Kinetics of Formation. *Adv. Mater.* **2005**, *17*, 728–731.
7. Terech, P.; de Geyer, A.; Struth, B.; Talmon, Y. Self-Assembled Monodisperse Steroid Nanotubes in Water. *Adv. Mater.* **2002**, *14*, 495–498.
8. Terech, P.; Friol, S.; Sangeetha, N.; Talmon, Y.; Maitra, U. Self-Assembled Nanoribbons and Nanotubes in Water: Energetic *vs*. Entropic Networks. *Rheol. Acta* **2006**, *45*, 435–443.
9. Marques, E. F.; Edlun, H.; La Mesa, C.; Khan, A. Liquid Crystals and Phase Equilibria of Binary Bile Salt-Water Systems. *Langmuir* **2000**, *16*, 5178–5186.
10. Wenseleers, W.; Vlasov, I. I.; Goovaerts, E.; Obraztsova, E.; Lobach, A. S.; Bouwen, A. Efficient Isolation and Solubilization of Pristine Single-Walled Nanotubes in Bile Salt Micelles. *Adv. Funct. Mat.* **2004**, *14*, 1105–1112.
11. Barone, P. W.; Baik, S.; Heller, D. A.; Strano, M. S. Near-Infrared Optical Sensors Based on Single-Walled Carbon Nanotubes. *Nat. Mater.* **2005**, *4*, 86–92.
12. Fagan, J. A.; Becker, M. L.; Chun, J.; Hobbie, E. K. Length Fractionation of Carbon Nanotubes Using Centrifugation. *Adv. Mater.* **2008**, *20*, 1609–1613.
13. Arnold, M. S.; Green, A. A.; Hulvat, J. F.; Stupp, S. I.; Hersam, M. C. Sorting Carbon Nanotubes by Electronic Structure Using Density Differentiation. *Nat. Nanotechnol.* **2006**, *1*, 60–65.
14. Baughman, R. H.; Zakhidov, A. A.; de Heer, W. A. Carbon Nanotubes—The Route Toward Applications. *Science* **2002**, *297*, 787–792.
15. Wang, F.; Dukovic, G.; Brus, L. E.; Heinz, T. F. The Optical Resonances in Carbon Nanotubes Arise from Excitons. *Science* **2005**, *308*, 838–841.
16. O'Connell, M. J.; Bachilo, S. M.; Huffman, C. B.; Moore, V. C.; Strano, M. S.; Haroz, E. H.; Rialon, K. L.; Boul, P. J.; Noon, W. H.; Kittrell, C.; *et al.* Band Gap Fluorescence from Individual Single-Walled Carbon Nanotubes. *Science* **2002**, *297*, 593–596.
17. Fagan, J. A.; Simpson, J. R.; Landi, B. J.; Richter, L. J.; Mandelbaum, I.; Bajpai, V.; Ho, D. L.; Raffaelle, R.; Hight Walker, A. R.; Bauer, B. J.; *et al.* Dielectric Response of Aligned Semiconducting Single-Wall Nanotubes. *Phys. Rev. Lett.* **2007**, *98*, 147402.
18. Wray, S.; Cope, M.; Delpy, D. T.; Wyatt, J. S.; Reynolds, E. O. R. Characterization of Near Infrared Absorption Spectra of Cytochrome aa3 and Hemoglobin for the Non-Invasive Monitoring of Cerebral Oxygention. *Biochim. Biophys. Acta* **1998**, *933*, 184–192.
19. Fagan, J. A.; Simpson, J. R.; Bauer, B. J.; De Paoli Lacerda, S. H.; Becker, M. L.; Migler, K.; Hight Walker, A. R.; Hobbie, E. K. Length Dependent Optical Effects in Single Wall Carbon Nanotubes. *J. Am. Chem. Soc.* **2007**, *129*, 10607–10612.
20. Heller, D. A.; Mayrhofer, R. M.; Baik, S.; Grinkova, Y. V.; Usrey, M. L.; Strano, M. S. Concomitant Length and Diameter Separation of Single-Walled Carbon Nanotubes. *J. Am. Chem. Soc.* **2004**, *126*, 14567–14573.
21. Crochet, J.; Clemens, M.; Hertel, T. Quantum Yield Heterogeneities of Aqueous Single-Wall Carbon Nanotube Suspensions. *J. Am. Chem. Soc.* **2007**, *129*, 8058–8059.
22. Tsyboulski, D. A.; Bachilo, S. M.; Weisman, R. B. Versatile Visualization of Individual Single-Walled Carbon Nanotubes with Near-Infrared Fluorescence Microscopy. *Nano Lett.* **2005**, *5*, 975–979.
23. Gittes, F.; Mickey, B.; Nettleton, J.; Howard, J. Flexural Rigidity of Microtubules and Actin Filaments Measured from Thermal Fluctuations in Shape. *J. Cell Biol.* **1993**, *120*, 923–934.
24. Brangwynne, C. P.; Koenderink, G. H.; Barry, E.; Dogic, Z.; MacKintosh, F. C.; Weitz, D. A. Bending Dynamics of Fluctuating Biopolymers Probed by Automated High-Resolution Filament Tracking. *Biophys. J.* **2007**, *93*, 346–359.
25. Duggal, R.; Pasquali, M. Dynamics of Individual Single-Walled Carbon Nanotubes in Water by Real-Time Visualization. *Phys. Rev. Lett.* **2006**, *96*, 246104.